Background Data for Validation

of the He-Torrance Model

Hongsong Li
Kenneth E. Torrance

TR-PCG-05-02 April 5, 2005

We present an experimental study of the angular distribution of light scattered from several rough metallic surfaces, which cover a range of roughness conditions. A BRDF model based on the Kirchhoff approximation was used to demonstrate the relation between surface-height statistics and the angular distribution of the scattered light. To do this, the angular distributions calculated with the BRDF model were fit to the measurements; the surface-height statistics were computed with a composite roughness model, and were used as inputs to obtain the BRDF predictions. We show that the Kirchhoff approximation can be applied to rough metallic surfaces that have multiple scales of roughness and near-, but not perfect, Gaussian surface-height distributions.

1. Introduction

The computer graphics (CG) community needs efficient analytical models to accurately describe the angular distribution of light scattered from a rough surface.[1] Physically-based models have been developed for this purpose, but the models need to be verified by experiments. To use a physically-based model, we also need a practical method to estimate the surface-roughness input parameters, based on surface height analyses or measurements on a surface. In this work, we will examine the usefulness of an existing reflectance model, which is based on the Kirchhoff approximation,[2,3] for roughened metallic surfaces and propose a method of surface-height characterization.

A. Analytical Models of Surface Bidirectional Reflectance for Computer Graphics Applications

The light scattering from rough surfaces has long been a subject of interest for the computer graphics (CG) community. The goal is to simulate the appearance of three-dimensional scenes in the real world. To do this, analytical models are used to describe the directional and spectral dependence of the reflectance over the entire angular domain and visible spectrum. The directional properties of the surface reflectance are usually characterized by the bidirectional reflectance distribution function (BRDF).[4]

For CG applications, a BRDF model should be efficient, accurate, and easy to use. First, the calculation of the BRDF values has to be efficient, because millions of BRDF evaluations are required to get quality images even for a scene with simple geometry and lighting conditions. We prefer analytical models that demand less computational power and have relatively simple

analytical expressions. Second, the BRDF model should cover the entire incident and reflection hemispheres, and over the entire visible wavelength range, with good accuracy. This requirement is necessary to render the appearance of surfaces under arbitrary orientations and lighting conditions, and for correct color reproduction. Third, the input parameters for the BRDF model should be intuitive and easy to determine.

Limited by computational power, the early BRDF models in CG emphasized efficiency more than accuracy and applicability, following an empirical apporach.[5~7] To improve the models, advancements from optics were introduced.[8-10] Among these, BRDF models employing the Kirchhoff approximation were promising due to their relative simplicity, analytical form, ease of computation, accuracy, and statistical representation of rough surfaces. The scalar form of the Kirchhoff approximation was developed by P. Beckmann[2] and a more general vector form by A. Stogryn[3]. The latter allows for a full Fresnel reflectivity and polarization. Based on the foregoing, X. He et. al. [10] proposed a comprehensive BRDF model (He-Torrance model hereafter) for CG applications. The model incorporates the vector form,[3] the masking/shadowing factor developed by B. G. Smith,[11] and applies for first-surface reflections. Any multiple scattering on the surface, or any possible subsurface scattering, were modeled with a constant Lambertian term. (More details on the He-Torrance model and the basic equations are available in Appendix A.) Since the He-Torrance model is based on the Kirchhoff approximation, the validity of that approximation will directly affect any predictions.

The limitations and accuracy of the Kirchhoff approximation have been studied theoretically and experimentally. Generally, the Kirchhoff approximation is accurate when the radius of surface

curvature (due to roughness elements, for example) is large compared with the illuminating wavelength and the angle of incidence is not large.[12] In addition, the accuracy may be limited by other assumptions of the theoretical model, such as a Gaussian distribution of surface heights, a single length scale of roughness, or a constant reflection coefficient.

B. Experimental Validation of Surface Bidirectional Reflectance Models

In the CG community, experimental tests of BRDF models are somewhat limited. Several BRDF instruments were built and used to validate models.[9,13-15] Perhaps the earliest BRDF measurements used by the CG community were published by K. E. Torrance and E. M. Sparrow.[26] Those measurements were adopted to develop what is now known in the field as the Cook-Torrance model[8] and the He-Torrance model.[10] Unfortunately, none of the measurements provided ample angular and spectral coverage. For validating the He-Torrance model, the experimental studies included only limited measurements of the surface-heights of the samples.

In the optics community, extensive experimental investigations of light scattering have been carried out to validate various BRDF models. One classic study is that of K. A. O'Donnell and E. R. Mendez,[19] who took great efforts to fabricate perfectly Gaussian-distributed surfaces with a single scale of roughness. The surfaces were fabricated by a lithography technique, which makes it possible to control the height statistics of the fabricated surfaces.[20] To validate the Kirchhoff approximation, the surface-heights of these surfaces were measured and analyzed. Next, the BRDFs of these surfaces were measured. Calculated directional reflectances based on the surface statistics agreed well with the measured reflectances. This success inspired more experimental work to study surfaces fabricated with similar techniques.[21-24] Although these "perfect" samples led to good agreement between the theory and the experimental results, the

applicability of the Kirchhoff approximation for real-world surfaces was still not verified, since such surfaces may not have near-Gaussian surface-height distributions or may have multiple scales of roughness.

Experimental studies of light scattering and surface-height statistics were also carried out for "less perfect" samples, such as aluminized ground glass,[25] magnesium oxide ceramic,[26] fused polycrystalline aluminum oxide,[27] hand-lapped stainless steel,[28] diamond-turned brass/nickel,[29] and epoxy coatings.[30] The agreement between theory and measurement was less satisfactory, compared with "perfect" surfaces. E. Marx and T. V. Vorburger[28] studied the relation between the surface-heights of hand-lapped stainless steel (measured with a stylus profilometer) and the angular distribution of light scattering (measured with a laser scatterometer). A theoretical model, which is based on the scalar form of the Kirchhoff approximation, was used to compute the scattering intensity with the height statistics; on the other hand, the model was also fit to the measurements to obtain the height statistics. Multiple scales of roughness were rarely considered, a fact that may partially explain the discrepancies between measured and calculated results.

One approach to describe the light scattering from rough surfaces with multiple roughness scales is to use composite roughness models. [16-18] Such models divide a rough surface into two independent components: a high-frequency small-scale roughness component riding on a low-frequency large-scale roughness component. The light scattered by these two components is treated separately by using either a perturbation or a Kirchhoff approach, depending on the height statistics. However, it is impractical to directly use the composite models for CG because

of their complexity. Another approach is to measure the surface-heights and to isolate the roughness scale (or the spatial bandwidth) that dominates scattering behavior. E. Marx and T. V. Vorburger[28] realized the importance of the spatial bandwidth selection. They filtered their surface-height data to attenuate spatial wavelengths > 50μm. The roughness statistics of the filtered data agreed better with that inferred by fitting a BRDF model to the optical measurements. However, this filtering technique did not have a theoretical basis.

The first purpose of the present paper is to provide measured data on light scattering with sufficient angular and spectral coverage for CG applications. Second, we want to examine the usefulness of the He-Torrance model for some real-world metallic surfaces. Third, a practical method is proposed to characterize such surfaces and to generate input roughness parameters for the He-Torrance model. The revised surface-height statistics can help to predict the angular distribution of scattered light for visual appearance simulations. For simplicity, we limit our effort to metallic surfaces and the visible light spectrum.

The paper starts in Section 2 with the fabrication and characterization of the test surfaces. In Section 3 we describe the reflection measurements. In Section 4 we present surface-height statistics and describe their relation to values needed for the He-Torrance model. In Section 5 we discuss experimental and predicted light scattering distributions.

2. Surface Preparation and Characterization

Five isotropic metallic surfaces were fabricated with three preparation methods, as described in Section 3A. In Section 3B, we present the surface-height measurements and a composite

roughness model to obtain height statistics that are meaningful to our applications. Tables 1 and 2 provide a list of the samples and some measured and inferred roughness statistics.

A. Preparation of Rough Surfaces

To determine how to fabricate test surfaces, we considered several factors. First, the finished surface of a formative process should represent a class of real-world surfaces. Second, we should understand the mechanism of the formative processes that create these test surfaces so that we can control the height statistics of the finished surfaces to some extent. Third, the formative process should be able to create a large (larger than 100mm×100mm), uniform (less than ±10% non-uniformity), and isotropic test surface, because at grazing angles of reflection the detector views a large area on the sample surface. We chose three methods of surface preparation: bead-blasting, grinding, and etching.

With bead-blasting, very small, perfectly round beads are propelled by high pressure air to remove/deform the top layer of a surface. This is a numerous, random, and cumulative process resulting in a Gaussian surface. An industrial bead-blaster was used (with glass beads of 0.25mm diameter). The air pressure was adjusted to fabricate surfaces with different roughness. Surfaces BBQAL1 and BBQAL2 were processed with air at 690kPa and 138kPa, respectively. The substrates of these test surfaces are Q-panels (R-46), a reference steel panel (100mm x 125mm) used for the paint and manufacturing industries. More than 10 minutes of blasting guaranteed the randomness of the process.

The second method, abrasive grinding, usually results in non-Gaussian surfaces. Since the surface-heights generated by this process are determined by the largest grinding grit, this process

is random but not cumulative. We used a BUEHLER NELSON-ZIMMER® 2000 system to grind two pieces of 125mm×125mm window glass. Grinding powders with two grit sizes, 120grit and 240grit, were used to fabricate test samples GGAL120 and GGAL240, respectively. More than five hours of grinding guaranteed the randomness and uniformity. A microscope was used to inspect the finished surfaces; the ground glass surfaces look "jagged."

The third method is etching, which may or may not result in a Gaussian surface. The uncertainty arises because the etching process is influenced by the material's microstructure. Therefore, etching is not completely random. The test sample, NGGAL, is commercial, acid-etched, non-glare glass (125mm×125mm).

A thin film of pure aluminum was deposited on each test surface with a CHA RAP-600 Thermal Evaporator. The film has a thickness of approximately 50nm, so that no light energy transmitted through the film. Thus, subsurface light scattering can be neglected.

B. Characterization of Rough Surfaces

A surface measurement instrument, a Tencor Alpha Step 500 Surface Profilometer, was used to measure the surface-heights (or profiles) of the test samples. This is a stylus-traversing instrument that provides $z(x)$ height data with 1-Angstrom vertical and 0.1μm horizontal resolutions. For each test surface, nine measurements were taken in randomly chosen regions and in random directions. Each height measurement consists of 4000 data points, which represents a 400μm traverse.

The height data were analyzed statistically. For a random rough surface, the vertical and horizontal height distributions can be respectively described by the height probability distribution function (PDF) and the spatial autocorrelation function (ACF). Though not normalized, the histogram of the height data can be used as the PDF. The ACF $\rho(\beta)$ is given by:

$$\rho(\beta) = \lim_{L\to\infty} \frac{\int_0^L z(x)z(x+\beta)dx}{\int_0^L z(x)^2 dx} \tag{1}$$

where L is the stylus traverse length. When both the PDF and the ACF conform to a Gaussian (normal) distribution, the surface is said to be Gaussian. The PDF and ACF are qualitative descriptions; we need both to evaluate a departure from Gaussian behavior. Quantitative measures of the PDF and ACF are respectively provided by the root mean square (RMS) roughness height σ and the horizontal autocorrelation length τ. Both are e-folding lengths associated with exponentials. The RMS roughness σ can also be obtained from:

$$\sigma = \sqrt{\frac{1}{L}\int_0^L z(x)^2 dx} \tag{2}$$

The slope of a rough surface is the ratio of the RMS roughness to the autocorrelation length, namely, σ/τ. These quantities are used as inputs for the He-Torrance and other BRDF models.

Care is required in interpreting these statistical measures, as real-world surfaces may have a wide range of roughness scales. Among them, only a limited range (of spatial bandwidths) are relevant here; in particular, only those dominating the directional light scattering.

Using computational studies of the light scattered from surfaces with multiple roughness length scales, Y. Yang and R. O. Buckius[32] determined that the roughness domain with the largest slope dominated the directional scattering distributions. This provides the basis for our roughness model. We assume that our measured surface-heights can be divided into two components: a high-frequency small-scale component and a low-frequency large-scale component. For our data, the high-frequency small-scale component turned out to have the highest slopes. We thus used a high-pass filter on our measured roughness data for each surface to filter out the large-scale components. The lengths of the large-scale components that were filtered out were about 25~40μm, varying from surface to surface. The shortest filter, $25\mu m$, is about 50 times the incident wavelength. Our filter length scales are close to the filter length used by E. Marx and T. V. Vorburger (50μm).[28]

The foregoing is illustrated graphically in Figure 1. The results of one measurement of *z(x)* for surface GGAL120 was divided into two components by filtering. Since the high-frequency small-scale component is expected to dominate the scattered light directional distributions, we focus on the statistics of that component. The low-frequency large-scale component will be neglected. Although this simplified approach will bring errors to the statistical results, we believe that the error is acceptable for our applications.

For each test sample we did similar separations. We calculated the RMS roughness σ and the autocorrelation length τ for the nine surface-height traverses, for the high-frequency small-scale component only (results are available in Appendix B). We also calculated the average and the standard deviation of σ to assess spatial uniformity. Similarly, we also calculated σ and τ from

the raw height data. Results for σ, τ and the slope σ/τ appear in Table 1. We selected the height measurements nearest the center of the surface to obtain the PDF and ACF graphs that are displayed later.

3. Reflectance Measurements

We measured BRDFs with a gonioreflectometer and directional-hemispherical reflectances with an Optronics OL-750 diffuse reflectometer. The procedures are described in Sections 3A and 3B. To illustrate some measured results, we will use Figures 2 to 4 which correspond to the bead-blasted steel surface BBQAL2.

A. Measuring BRDF

The BRDF is the ratio of the radiance reflected from a surface in the direction (θ_r, ϕ_r) to the irradiance onto the surface from the direction (θ_i, ϕ_i).

$$f_r(\lambda, \theta_i, \phi_i, \theta_r, \phi_r) = \frac{dL_r(\lambda, \theta_i, \phi_i, \theta_r, \phi_r)}{dE_i(\lambda, \theta_i, \phi_i)} \tag{3}$$

where λ is the wavelength, θ_i and ϕ_i are the zenith and azimuthal angles of the irradiance, and θ_r and ϕ_r are the zenith and azimuthal angles of the reflected radiance. The coordinate system is shown in Appendix A. For an isotropic surface, only three angles are needed. The reflected radiance dL_r and irradiance dE_i have units of W/m^2sr and W/m^2, respectively.

An automated, three-axis BRDF measurement instrument, called a gonioreflectometer, was built in the Optical Measurement Laboratory at the Cornell Program of Computer Graphics.[33-35] The gonioreflectometer performs rapid measurements of the BRDF of flat, isotropic sample surfaces over the visible spectrum and over most of the incident and reflection hemispheres. Special

design was applied to enable BRDF measurements at grazing angles up to 85°. The spectroradiometric detector takes 31 convolved wavelength samples covering the visible spectrum (400nm-700nm) in one snapshot. For the measurements on our rough metallic surfaces, the BRDF values were obtained by a relative method, which compared the reflected signal from our test surfaces with that from a reference surface (Spectralon) with a known BRDF.

The flexible sampling mechanism of the gonioreflectometer enables us to sample the BRDFs in the plane of incidence, as well over the entire reflection hemisphere. Figure 2 shows BRDF measurements in the plane of incidence for various illumination angles θ_i. We also measured the BRDFs at uniformly-distributed sampling positions over the reflection hemisphere. For an incident direction of 10° and a wavelength of 550nm, the BRDF in the reflection hemisphere is shown in Figure 3. The vertical axis is the BRDF; the left and right orthogonal axes map the spherical coordinates above a surface. The plane of incidence corresponds to 0 on the left axis. The points are plotted in a uniform parameterization of the hemisphere such that each grid element in the plot represents a region of the hemisphere with the same solid angle.[35]

B. Measuring Directional-hemispherical Reflectance

The directional-hemispherical reflectance ρ_{dh} is the ratio of the radiant power dE_r reflected to the hemisphere to the radiant power dE_i incident onto a surface, both in W/m^2; ρ_{dh} can also be derived by integrating the BRDF over the reflection hemisphere:

$$\rho_{dh}(\lambda,\theta_i,\phi_i) = \frac{dE_r}{dE_i} = \int_{\Omega_r} f_r(\lambda,\theta_i,\phi_i,\theta_r,\phi_r)\cos\theta_r d\Omega_r \qquad (4)$$

where the integral is over the reflection hemisphere Ω_r. The integral is bounded by unity due to energy conservation.

The OL750 system directly measured the directional-hemispherical reflectance ρ_{dh} (the left side of (4)) for a flat surface at an incidence angle of 10° with a rated error of less than 1%. On the other hand, the BRDFs measured by the gonioreflectometer at an incident direction of 10° were numerically integrated over the reflection hemisphere (the right side of (4)) to obtain the directional-hemispherical reflectances. Figure 4 shows a comparison of the integrated and directly-measured ρ_{dh} for the surface BBQAL2. (Note: both instruments used Spectralon as their common reference surface.) In Figure 4, over the entire visible spectrum, the directional-hemispherical reflectance obtained from the integrated BRDF measurements is within 2% of the comparison values obtained by direct measurement with the OL-750 system. The only exception is at short wavelengths, below 420nm. The comparison suggests that the BRDF measurements are accurate in both magnitude and spectrum, with less than 2% integrated error.

For all the test surfaces, we measured the BRDFs in the plane of incidence and over the reflection hemisphere. With the OL750 measurement data, we confirmed that the accuracy of the BRDF measurements is generally within 2%. For CG applications, the measurements provide sufficient accuracy as well as ample angular and spectral coverage. Subsequently, the BRDF measurements are used to study the relation between surface roughness statistics and light scattering behavior. Measured results for all five rough metallic samples are presented in Section 5. Limited by space, only representative results are shown.

4. Relating Surface-height Statistics to the Angular Distribution of Scattered Light

The relation between surface-height statistics and the angular distribution of light reflected from a surface leads to inverse and direct scattering problems. The inverse problem is to fit a model (in this case, the He-Torrance model) to the BRDF measurements to obtain the surface-height statistics; the direct problem is to predict the BRDF of a surface from a given set of surface-height statistics.

We start with the inverse problem. The performance of the data fitting helps us to evaluate the applicability of the model. For a metallic surface, the He-Torrance model[10] contains five parameters: wavelength λ, RMS roughness σ, autocorrelation length τ, index of refraction $n(\lambda)$, and a uniform-diffuse term $a(\lambda)$ (which allows for multiple surface scattering and/or subsurface scattering). Two of these parameters are either independently specified (λ) or found from tables ($n(\lambda)$).[37] For the roughness range of our metallic surfaces, the BRDF is determined predominantly by the roughness slope parameter (σ/τ). Thus, we need to find only the values of the slope (σ/τ) and uniform-diffuse ($a(\lambda)$) parameters to achieve a fit. As an upper-bound fitting constraint, we used the directional-hemispherical reflectance value (equation (4)) found by integrating the Fresnel reflectivity for polished, pure aluminum.

We used the nonlinear optimization function of Matlab which varies model parameters to minimize the fitting error between model and measured data. We used an energy-weighted root mean square fitting error:

$$\sigma_{fitting} = \sqrt{\frac{1}{N}\sum\{[f_{r,\mathrm{model}}(\lambda,\theta_i,\theta_r,\phi_r) - f_{r,measurements}(\lambda,\theta_i,\theta_r,\phi_r)]\times\cos(\theta_r)\}^2} \qquad (5)$$

The functions f (model and measured) depend on four independent variables $(\lambda, \theta_i, \theta_r, \phi_r)$ which span the measurement space. For simplicity, we elected to fit only at the midpoint of the visible spectrum (λ = 550nm). The cosine term in (5) gives smaller weights to BRDF values at large grazing angles of reflection, where the absolute BRDF values can be several orders of magnitude larger than those in other parts of the reflection hemisphere. Otherwise, the large-magnitude differences in the BRDF values can bias a fitting. The fitting method appears to be robust and was independent of the initial values.

The direct problem is solved by employing the surface height statistics found by mechanical measurement in Section 2. Of course, there are intrinsic errors in those measurements and also some variations over the surface due to surface non-uniformities. We allow for this and later provide upper and lower bounds for directly-calculated BRDFs from the model.

It is generally complicated to do rigorous data fitting for a nonlinear function like the BRDF. However, for our applications in CG we are allowed to relax some of those concerns, due to limitations in human vision, cameras, and display devices, such as polarization insensitivity and limited dynamic range. As a result, some effects like narrow retro-reflections and de-polarization can often be neglected; and the relative errors in BRDF predictions at very low or very high absolute magnitudes may not be perceptible to the eye. However, human vision is sensitive to surface glossiness, which affects the lateral shape and angular positions of the reflectance lobe, so these features should be accurately predicted by a reflectance model.

5. Experimental Results

Results for the aluminized bead-blasted steel panels, the aluminized ground glass, and the aluminized acid-etched glass are given in the following sections. Since the reflecting metal, aluminum, has an almost flat reflectance spectrum over the visible region, we present results only for a single wavelength, $\lambda = 550$nm.

A. Bead-blasted Steel Panels with Aluminum Coating

For the two bead-blasted steel surfaces, BBQAL1 (roughest) and BBQAL2 (smoothest), the normalized height histograms and the autocorrelation functions (ACF) for the high-frequency small-scale component of the roughness are shown in Figure 5. The solid lines are the fit of Gaussian curves. For the histograms, the curves agree moderately well with the data, suggesting that the high-frequency small-scale component of the roughness is nearly Gaussian. For the autocorrelation functions ACF, the fitted curves agree very well with the data. Considering the random characteristics of the bead-blasting process, these results are understandable.

Reflectance measurements for the two bead-blasted steel surfaces, BBQAL1 and BBQAL2, are presented in Figures 6 to 10; of these, Figures 6, 7, 9, and 10 are incidence-plane BRDFs, whereas Figure 8 displays BRDFs in the hemisphere. In the incidence-plane figures, the curves are results from the model. In Figures 6 and 7, the curves are the best-fit curves; in Figures 9 and 10, the same measured data are shown, but the curves are calculated using the measured slopes (σ/τ) for the small-scale roughness as inputs to the model. The upper/lower bounds were found by varying the input slopes by +/- amounts corresponding to the measured percentage non-uniformity in the roughness of the surface (see Table 1).

Results for the roughest (σ=0.72μm) and smoothest (σ=0.54μm) bead-blasted metal surfaces are shown, respectively, in Figures 6 and 7. The roughness to wavelength ratios are of order one, so a wave optics model is appropriate. Note the good agreement between the model and the measurements. A similar comparison over the reflection hemisphere is shown in Figure 8 for the rougher surface.

For small angles of incidence (10°and 30°), the measurements shown in Figures 6 and 7 are Gaussian-like curves with maxima near or just beyond the specular angle. For 60° incidence, off-specular maxima are apparent. Best-fit slope values for Figures 6 and 7 are 0.144 and 0.080, respectively. On the other hand, measured values for the high-frequency small-scale surface roughness component yield 0.129 and 0.084, respectively. The former is 10% low and the latter is 4% high. If we also compare to slope values from the raw height data (before scale separations), we have slope values of 0.095 and 0.041, which are respectively 30% low and 50% low as compared to the best-fit values. The raw data values reflect the influence of the gentler slopes of the large-scale roughness components. The closer agreement of the best-fit and mechanically-measured high-frequency small-scale roughness slopes strongly suggests the value of scale separation when trying to use mechanical roughness measurements as input to a model.

For the bead-blasted steel surfaces, an alternative display of the measured data (in Figures 6 and 7) is presented as a sensitivity study in Figures 9 and 10. As noted earlier, the curves are calculated from the reflection model using slope values (σ/τ) that bound the variability in the measured small-scale roughness slopes (σ/τ) . Accordingly, the measured slope of 0.129 for the

roughest surface was varied by ± 3.9% in Figure 9 to get the upper and lower curves. Similarly, the measured slope of 0.084 for the smoothest surface was varied by ± 6.8% in Figure 10.

In Figure 9, the model results fall below the measurements. Indeed, the best fit inferred slope for this surface is about 10% higher. In Figure 10, on the other hand, upper/lower model results tend to bracket the measurements.

The He-Torrance model appears to work very well for the bead-blasted steel surfaces. This is not a surprise since the surfaces have height distributions and autocorrelation functions close to Gaussian. Moreover, the small-scale roughness statistics appear to be more reasonable to use than those of the raw height data.

B. Ground Glass with Aluminum Coating

For the two ground glass surfaces, GGAL120 (roughest) and GGAL240 (smoothest), the histograms and the autocorrelation functions (ACF) for the high frequency small-scale component of the roughness are shown in Figure 11. The fitted Gaussian curves agree moderately well suggesting that the high-frequency small-scale roughness components are nearly Gaussian. However, the grinding process itself implies that the roughness should not be Gaussian. To explain this, the height histogram and ACF for the raw height data of surface GGAL120 are shown in Figure 12. The associated histogram is nearly Gaussian but slightly skewed to the right toward higher heights, consistent with a grinding process that removes more peaks than valleys. On the other hand, the associated autocorrelation function is rather more exponentially distributed than Gaussian. This is consistent with the "jagged" appearance observed under a microscope. The statistical data imply that a ground glass surface consists of a high-frequency, small-scale Gaussian roughness component (statistics in Figure 11) superposed

on a low-frequency large-scale "jagged" roughness component. The small-scale roughness is expected to dominate the light scattering.

Incidence-plane BRDF measurements and data fitting results are shown for the roughest (σ=0.86μm) and smoothest (σ=0.61μm) rough glass surfaces, GGAL120 and GGAL20, respectively, in Figures 13 and 14. A similar comparison over the reflection hemisphere is shown in Figure 15 for the rougher surface. Incidence-plane BRDF measurements and results from the model using the measured small-scale roughness slopes are shown in Figures 16 and 17; upper/lower estimates reflect the measured non-uniformity of the surface.

Results in Figures 13 and 14 are nearly identical because the high-frequency small-scale roughness values are very similar for the two surfaces (Table 1). The BRDFs show a Gaussian-like curve only for 10° incidence. An off-specular peak is apparent for higher angles of incidence. The fittings of the He-Torrance model to the reflectance data are generally good except that the model overestimates the magnitude of the off-specular peaks at incidence angles of 60° and higher. The errors are mainly due to shadowing/masking effects from one term in the model. A better shadowing/masking factor could reduce those errors. The "jagged" large-scale roughness only makes the effects more apparent. The best-fit slope value from the data fitting in Figure 13 is 0.166, about 8% higher than the measured value of 0.154 (for the high-frequency small-scale roughness component). The best-fit slope value for Figure 14 is 0.158, about 20% higher than the measured slope of 0.130. For the two figures, the slopes calculated from the raw height data are 0.064 and 0.068, respectively, for Figures 13 and 14, even though the raw height data indicate very different surface roughness (σ=2.66μm vs. σ=1.63μm).

Thus, the BRDF measurements for the two ground glass samples are surprisingly close, even though their raw height surface roughnesses are very different. The similarity of the measurements suggests that the small-scale structures of the two surfaces are quite similar. That is confirmed by the data fitting, since early equal small-scale slopes were inferred. The large-scale roughness of the two surfaces, though quite different, has little influence on the angular distribution of the scattered light. For completeness, the effects of surface non-uniformity may be inferred from Figures 16 and 17, where it is clear that the measured slopes (σ/τ) yield BRDF predictions that fall somewhat above the best-fit predictions in Figures 13 and 14.

The He-Torrance model has a relatively good performance with the ground-glass surfaces. Although the fitting results are not as satisfactory as those for the bead-blasted surfaces, the model predicts the off-specular peaks with moderate magnitude errors.

C. Acid-etched Glass with Aluminum Coating

The aluminized acid-etched glass is much smoother than the other test surfaces (Table 1). On the other hand, the surface is sufficiently rough so that no mirror reflection can be observed except at high grazing angles of incidence. The small-scale roughness is very close to Gaussian, as shown in Figure 18. Therefore, good comparisons with the He-Torrance model are expected.

Incidence-plane BRDF measurements and data fitting are shown in Figures 19 and 20. The latter figure uses a logarithmic ordinate to better display the dynamic range of the BRDF, since there is virtually no diffusely scattered light. Also, no off-specular peak is observed due to the gentle slope of the surface-heights. The fittings of the data to the He-Torrance model are very good,

except that the model slightly underestimates the maximum reflectance in the specular direction for large angles of incidence (more than 60°). The slope value obtained from the data fitting is 0.02, about 15% lower than the measured value of 0.024 (for the small-scale roughness component). The slope calculated from the raw heights data is approximately 0.018, which is very close to the slope obtained with the scale separation. By doing a sensitivity study, and varying the mechanically-measured slope (σ/λ=0.024) by the observed surface non-uniformity (5.3%), the resulting upper and lower bounds essentially bracket the data in Figure 21.

The He-Torrance model works well for this acid-etched glass surface. The positions and the lateral shapes of the reflection lobes are accurate. The underestimation of the maximum BRDF values is acceptable for our applications due to the limited dynamic ranges of human vision and display devices. Our surface characterization method is less necessary in this case. Although the measured slope is close to the fitting result, the improvement is not significant. The height statistics suggest that this surface may have only a single scale of roughness.

6. Conclusion

In this work, we experimentally study the relation between the surface-height statistics and the angular distribution of the first-surface light scattering from several rough metal surfaces. The surface-heights were measured with a surface profilometer; the BRDFs of the surfaces were measured with a gonioreflectometer.

An analytical model based on the Kirchhoff approximation, the He-Torrance model,[10] was fit to the measured BRDFs of the rough metal surfaces. The fittings show that the model is able to describe the first-surface scattering of rough metallic surfaces that have multiple scales of

roughness and near-Gaussian surface-height distributions, with an accuracy sufficient for computer graphics applications. The good agreement between the model and measurements implies that only one scale of roughness dominates the light scattering behavior.

The light scattering distributions are primarily attributable to the steepest-slope surface-roughness components.[32] We propose a composite roughness model, and with a filter, we extract the steepest-slope components from the surface profilometer measurements. Using the statistics of that component (i.e., the roughness slope σ/τ) as input to the He-Torrance model, satisfactory agreement with the measured BRDFs was observed for our rough metal surfaces. The approach provides computer graphics practitioners with a practical method to obtain the input roughness data for use with a physical-optics-based light reflection model.

Acknowledgements

The authors would like to thank Professor Donald Greenberg, Steve Westin, and Hurf Sheldon of the Cornell Program of Computer Graphics for their encouragement and technical support. Equipment was donated by the Imaging Science Division of Eastman Kodak (Larry Iwan) and the Hewlett-Packard Company. This research was supported by the NSF Information Technology Research Program (ACI-0113851), the NSF Science and Technology Center for Computer Graphics and Scientific Visualization (ASC-8920219), the NSF Cornell Center for Materials Research (DMR-0079992) and the NSF Thermal Systems Program (CTS-9213183).

References

1. D. P. Greenberg, K. E. Torrance, F. X. Sillion, J. Arvo, J. A. Ferwerda, S. Patanaik, E. P. F. Lafortune, B. Walter, S. C. Foo, and B. Trumbore, "A framework for realistic image synthesis," Comput. Graph. Proc., Annual Conference Series (SIGGRAPH95), 477-494 (1995).
2. P. Beckmann and A. Spizzichino, "The scattering of electromagnetic waves from rough surfaces," Pergamon Press, Oxford, UK, 1963.
3. A. Stogryn, "Electromagnetic scattering from rough, finitely conducting surfaces," Radio Sci. **2(4)**, 415-428, 1966.
4. F. E. Nicodemus, "Reflectance nomenclature and directional reflectance and emissivity," Appl. Opt. **9**, 1474-1475, 1970.
5. B. T. Phong, "Illumination for computer generated pictures," Communications of the ACM **18(6)**, 311-317, 1975.
6. J. F. Blinn, "Models of light reflection for computer synthesized pictures," *Comput. Graph.* **11** (SIGGRAPH77), 192-198, 1977.
7. E. P. F. Lafortune, S. C. Foo, K. E. Torrance, and D. P. Greenberg, "Non-linear approximation of reflectance functions," Comput. Graph. Proc., Annual Conference Series (SIGGRAPH97), 117-126 (1997).
8. R. L. Cook and K. E. Torrance, "A reflectance model for computer graphics", ACM Trans. Graph. **1**, 7-24, 1982.
9. G. J. Ward, "Measuring and modeling anisotropic reflection," *Comput. Graph.* **26** (SIGGRAPH92), 265-272, 1992.

10. X. D. He, K. E. Torrance, F. X. Sillion, and D. P. Greenberg, "A comprehensive physical model for light reflection," *Comput. Graph.* **25** (SIGGRAPH91), 175-186, 1991.
11. B. G. Smith, Geometrical shadowing of a random rough surface," IEEE Trans. Ant. Prop. **AP-15**, 668-671, 1967.
12. E. I. Thorsos, "The validity of Kirchhoff approximation for rough surface scattering using a Gaussian roughness spectrum," J. Acoust. Soc. Am. **83**, 78-92, 1988.
13. S. Marschner, S. Westin, E. Lafortune, and K. Torrance, "Image-based measurement of the bidirectional reflectance distribution function," *Applied Optics* 39, 16, 2592-2600, 2000.
14. K. J. Dana, "BRDF/BTF measurement device," in Proceedings of the International Conference on Computer Vision (IEEE Computer Society Press, Los Alamitos, Calif., 2001), 460-466, 2001.
15. W. Matusik, H. P. Pfister, M. Brand, and L. McMillan, "A data-driven reflectance model," *ACM Transactions on Graphics*, v. 22, 3, 759-769, 2003.
16. G. R. Valenzuela, "Scattering of electromagnetic waves from a tilted slightly rough surface," Radio Sci. **3**, 1057-1066, 1968.
17. G. S. Brown, "Backscattering from a Gaussian-distributed perfectly conducting rough surface," IEEE Trans. Ant. Prop. **AP-26**, 472-482, 1978.
18. S. T. McDaniel and A. D. Gorman, "An examination of the composite-roughness scattering model," J. Acoust. Soc. Am. **73**, 1476-1486, 1983.
19. K. A. O'Donnell and E.R. Mendez, "Experimental study of scattering from characterized random surfaces", J. Opt. Soc. Am. A **4**, 1194-1205, 1987.
20. P. F. Gray, "A method of forming optical diffusers of simple known statistical properties," Opt. Acta **25**, 765-775 (1978).

21. M. –J. Kim, J. C. Dainty, A. T. Friberg, and A. J. Sant, "Experimental study of enhanced backscattering from one- and two-dimentional random rough surfaces," J. Opt. Soc. Am. A. **7**, 569-577, 1990.
22. M. E. Knotts, and K. A. O'Donnell, "Measurement of light scattering by a series of conducting surfaces with one-dimensional roughness," J. Opt. Soc. Am. A. **11**, 697-710, 1994.
23. J. Q. Lu, J. A. Sánchez-Gil, E. R. Méndez, Z.-H. Gu, and A. A. Maradudin, "Scattering of light from a rough dielectric film on a reflecting substrate: diffuse fringes." J. Opt. Soc. Am. A **15**, 185-195, 1998.
24. E. I. Chaikina, A. G. Navarrete, E. R. Méndez, A. Martínez, and A. A. Maradudin, "Coherent scattering by one-dimensional randomly rough metallic surfaces," Appl. Opt. **37**, 1110-1121, 1998.
25. H. E. Bennett, "Specular reflectance of aluminized ground glass and the height distribution of surface irregulatities," J. Opt. Soc. Am. **53**, 1389-1394, 1963.
26. K. E. Torrance and E. M. Sparrow, "Theory for off-specular reflection from roughened surfaces," J. Opt. Soc. Am. **57**, 1105-1114 (1967).
27. D. H. Hensler, "Light scattering from fused polycrystalline aluminum oxide surfaces," Appl. Opt. **11**, 2522-2528, 1972.
28. E. Marx and T. V. Vorburger, "Direct and inverse problems for light scattered by rough surfaces," Appl. Opt. **29**, 3613-3626, 1990.
29. L. –X. Cao, T. V. Vorburger, A. G. Lieberman, and T. R. Lettieri, "Light-scattering measurement of the rms slopes of rough surfaces," Appl. Opt. **30**, 3221-3227, 1991.

30. M. E. McKnight, T. V. Vorburger, E. Marx, M. E. Nadal, P. Y. Barnes, and M. A. Galler, "Measurements and predictions of light scattering by clear coatings," Appl. Opt. **40**, 2159-2168, 2001.
31. T. R. Thomas, "Rough surfaces," Longman Press, London UK; New York, USA, 1982.
32. Y. Yang and R. O. Buckius, "Surface length scale contributions to the directional and hemispherical emissivity and reflectivity," Journal of Thermophysics and heat transfer **9(4)**, 653-659, 1995.
33. S. C. Foo, "A gonioreflectometer for measuring the bidirectional reflectance of material for use in illumination computation," M.S. thesis (Cornell University, Ithaca, NY, 1997).
34. H. Li and K. E. Torrance, "Validation of the Gonioreflectometer", Technical Report PCG-03-2 (Program of Computer Graphics, Cornell University, Ithaca, NY, 2003).
35. H. Li, S. C. Foo, K. E. Torrance, and S. E. Westin, "Automated three-axis gonioreflectometer for computer graphics applications," submitted to SPIE 2005.
36. P. Shirley and K. Chiu, "Notes on adaptive quadrature on the hemisphere," Technical Report 441 (Department of Computer Science, Indiana University, Bloomington, IN, 1994).
37. E. D. Palik, "Handbook of optical constants of solids," Academic Press, London, UK, 1998.

Appendix A: He-Torrance BRDF Model

The He-Torrance BRDF model is based on the vector form of the Kirchhoff approximation, describing the specular, directionally diffuse, and uniformly diffuse scattering behaviors. The angular distributions of the scattered light depend on wavelength, incident angles, two roughness parameters, and indices of refraction. The model applies for a wide range of materials and surface finishes. The coordinate system is shown in the following figure.

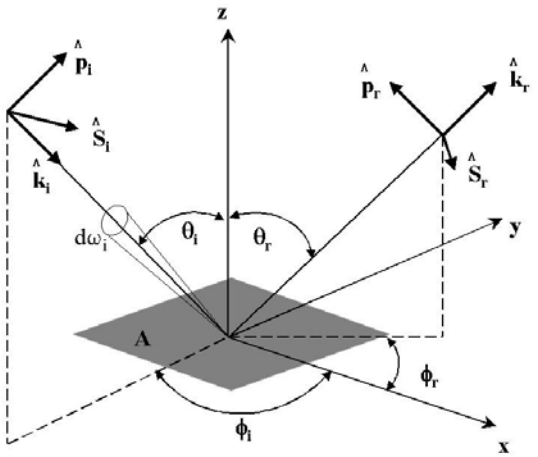

Coordinate system

Where A is the projected area of the surface; $\hat{k}$ is unit vector in wave direction; $\hat{s}, \hat{p}$ are *s* and *p* polarization unit vectors respectively.

Assumptions of the model:

- Local radius of curvature of the surface is large compared to the illuminating wavelength;
- Both surface-heights and autocorrelation function are Gaussian distributed;
- A single roughness length scale;
- Plane, uniform, and isotropic surfaces.

Equations:

$$\rho_{bd} = \rho_{bd}(\lambda, \sigma_0, \tau, \overline{n}(\lambda), a(\lambda)) = \rho_{bd,sp} + \rho_{bd,dd} + \rho_{bd,ud} \tag{6}$$

The specular reflection term: $\rho_{bd,sp} = \frac{\rho_s}{\cos\theta_i d\omega_i} \cdot \Delta$; (7)

The directional diffuse term: $\rho_{bd,dd} = \frac{|F|^2}{\pi} \cdot \frac{G \cdot S \cdot D}{\cos\theta_i \cos\theta_r}$; (8)

The uniformly diffuse term: $\rho_{bd,ud} = a(\lambda)$; (9)

$$\rho_s = |F|^2 \cdot e^{-g} \cdot S \tag{10}$$

$$\Delta = \begin{cases} 1, \text{if in specular cone} \\ 0, \text{otherwise} \end{cases} \tag{11}$$

$$|F|^2 = \frac{1}{2}(F_s^2 + F_p^2) = f(\theta_i, \theta_r \overline{n}(\lambda)) \tag{12}$$

$$G = (\frac{\lambda}{2\pi}\frac{\vec{v}\cdot\vec{v}}{v_z})^2 \cdot \frac{1}{\left|\hat{k}_r \times \hat{k}_i\right|^4} \cdot [(\hat{s}_r \cdot \hat{k}_i)^2 + (\hat{p}_r \cdot \hat{k}_i)^2] \cdot [(\hat{s}_i \cdot \hat{k}_r)^2 + (\hat{p}_i \cdot \hat{k}_r)^2] \tag{13}$$

$$S = S_i(\theta_i) \cdot S_r(\theta_r) \tag{14}$$

$$S_i(\theta_i) = (1 - \frac{1}{2} erfc(\frac{\tau\cot\theta_i}{2\sigma_0}))/(\Lambda(\cot\theta_i) + 1) \tag{15}$$

$$S_r(\theta_r) = (1 - \frac{1}{2} erfc(\frac{\tau\cot\theta_r}{2\sigma_0}))/(\Lambda(\cot\theta_r) + 1) \tag{16}$$

$$\Lambda(\cot\theta) = \frac{1}{2}\{\frac{2}{\pi^{1/2}} \cdot \frac{\sigma_0}{\tau\cot\theta} \cdot \exp[-(\frac{\tau\cot\theta}{2\sigma_0})^2] - erfc(\frac{\tau\cot\theta}{2\sigma_0})\} \tag{17}$$

$$D = \frac{\pi^2\tau^2}{4\lambda^2} \cdot \sum_{m=1}^{\infty} \frac{g^m e^{-g}}{m!\cdot m} \cdot \exp(-\frac{v_{xy}^2 \tau^2}{4m}) \tag{18}$$

$$g = [\frac{2\pi\sigma}{\lambda}(\cos\theta_i + \cos\theta_r)]^2 \tag{19}$$

$$\sigma = \sigma_0 \cdot [1 + (\frac{z_0}{\sigma_0})^2]^{-1/2} \tag{20}$$

$$\sqrt{\frac{\pi}{2}} z_0 = \frac{\sigma_0}{4}(K_i + K_r) \cdot \exp(-\frac{z_0^2}{2\sigma_0^2}) \tag{21}$$

$$K_i = \tan\theta_i \cdot erfc(\frac{\tau}{2\sigma_0}\cot\theta_i),\ K_r = \tan\theta_r \cdot erfc(\frac{\tau}{2\sigma_0}\cot\theta r) \tag{22}$$

$$\vec{v} = \frac{2\pi}{\lambda}(\hat{k}_r - \hat{k}_i) = v_x\hat{x} + v_y\hat{y} + v_z\hat{z},\ v_{xy} = \sqrt{v_x^2 + v_y^2} \tag{23}$$

$$\hat{s}_i = \frac{\hat{k}_i \times \hat{n}}{\left|\hat{k}_i \times \hat{n}\right|}, \quad \hat{p}_i = \hat{s}_i \times \hat{k}_i \tag{24}$$

$$\hat{s}_r = \frac{\hat{k}_r \times \hat{n}}{\left|\hat{k}_r \times \hat{n}\right|}, \quad \hat{p}_r = \hat{s}_{ri} \times \hat{k}_r \tag{25}$$

where $\overline{n}$ is the index of refraction, ρ_s is the specular reflectivity, Δ is a delta function, $|F|^2$ is the Fresnel reflectivity for unpolarized light evaluated at the bisecting angle given by $\cos^{-1}(|\widehat{k}_r - \widehat{k}_i|/2)$, G is a geometrical factor, S is the shadowing/masking factor, and D is a distribution function for the directional-diffuse reflection term.

Appendix B: The Statistics of High-frequency, Small-scale Roughness Component

For each test surface, nine mechanical surface scans were carried out in randomly chosen regions and in random directions. For each scan, we extracted the high-frequency, small-scale roughness components of the surface height data with a high-pass filter. The statistics of the small-scale components are summarized in Table 3~7.

Table 1: Summary of Measured Height Statistics

Surface	Raw height data			Small-scale roughness			
	[μm]	[μm]	σ/τ	[μm]	[μm]	σ/τ	Non-uniformity
BBQAL1, Aluminized Bead-blasted Steel	2.58	27.2	0.095	0.72	5.6	0.129	3.9%
BBQAL2, Aluminized Bead-blasted Steel	1.24	30.5	0.041	0.54	6.5	0.084	6.8%
GGAL120, Aluminized Ground Glass, 120grit	2.66	41.6	0.064	0.86	5.6	0.154	4.5%
GGAL240, Aluminized Ground Glass, 240grit	1.63	24.0	0.068	0.61	4.7	0.130	4.1%
NGGAL, Aluminized Acid-etched Glass	0.21	11.7	0.018	0.13	5.4	0.024	5.3%

Table 2: Summary of Data Fitting Results

Surface	Slope σ/τ	Uniform diffusive term, a
BBQAL1, Aluminized Bead-blasted Steel	0.144	0.70
BBQAL2, Aluminized Bead-blasted Steel	0.080	0.37
GGAL120, Aluminized Ground Glass, 120 grit	0.166	0.44
GGAL240, Aluminized Ground Glass, 240 grit	0.158	0.44
NGGAL, Aluminized Acid-etched Glass	0.02	0.0

Table 3: Statistics of small scale roughness component for BBQAL1, aluminized bead-blasted steel surface; filter size was 30μm

Scan #	RMS Roughness σ [μm]	Autocorrelation Length τ [μm]	Slope σ/τ
1	0.680	5.754	0.118
2	0.707	5.936	0.119
3	0.734	5.115	0.144
4	0.731	5.662	0.129
5	0.736	5.592	0.132
6	0.702	5.623	0.125
7	0.774	5.609	0.138
8	0.745	5.587	0.133
9	0.708	5.910	0.120
AVERAGE	0.724	5.643	0.129
STDEV	0.028	0.239	0.009
Non-uniformity	0.039		

Table 4: Statistics of small scale roughness component for BBQAL2, aluminized bead-blasted steel surface; filter size was 26μm

Scan #	RMS Roughness σ [μm]	Autocorrelation Length τ [μm]	Slope σ/τ
1	0.529	6.692	0.079
2	0.490	6.399	0.077
3	0.554	6.215	0.089
4	0.534	6.610	0.080
5	0.512	6.706	0.080
6	0.527	6.366	0.082
7	0.580	6.443	0.089
8	0.612	6.540	0.094
9	0.529	6.360	0.083
AVERAGE	0.541	6.481	0.084
STDEV	0.037	0.167	0.006
Non-uniformity	0.068		

Table 5: Statistics of small scale roughness component for GGAL120, aluminized ground glass; filter size was 34*μm*

Scan #	RMS Roughness σ [μm]	Autocorrelation Length τ [μm]	Slope σ/τ
1	0.860	5.607	0.153
2	0.889	5.725	0.155
3	0.798	5.812	0.137
4	0.870	5.518	0.158
5	0.888	5.628	0.158
6	0.835	5.570	0.150
7	0.900	5.581	0.161
8	0.880	5.764	0.153
9	0.797	5.453	0.146
AVERAGE	0.857	5.628	0.152
STDEV	0.039	0.118	0.007
Non-uniformity	0.045		

Table 6: Statistics of small scale roughness component for GGAL240, aluminized ground glass; filter size was 28*μm*

Scan #	RMS Roughness σ [μm]	Autocorrelation Length τ [μm]	Slope σ/τ
1	0.611	4.518	0.135
2	0.597	4.796	0.124
3	0.560	4.605	0.122
4	0.590	4.669	0.126
5	0.650	4.570	0.142
6	0.627	4.757	0.132
7	0.614	4.724	0.130
8	0.601	4.599	0.131
9	0.608	4.725	0.129
AVERAGE	0.606	4.663	0.130
STDEV	0.025	0.094	0.006
Non-uniformity	0.041		

Table 7: Statistics of small scale roughness component for NGGAL, aluminized acid-etched glass; filter size was 34*μm*

Scan #	RMS Roughness σ [μm]	Autocorrelation Length τ [μm]	Slope σ/τ
1	0.118	5.415	0.022
2	0.124	5.181	0.024
3	0.128	5.451	0.024
4	0.129	5.421	0.024
5	0.140	5.468	0.026
6	0.121	5.463	0.022
7	0.120	5.277	0.023
8	0.126	5.312	0.024
9	0.123	5.316	0.023
AVERAGE	0.125	5.367	0.023
STDEV	0.007	0.100	0.001
Non-uniformity	0.053		

List of Figures:

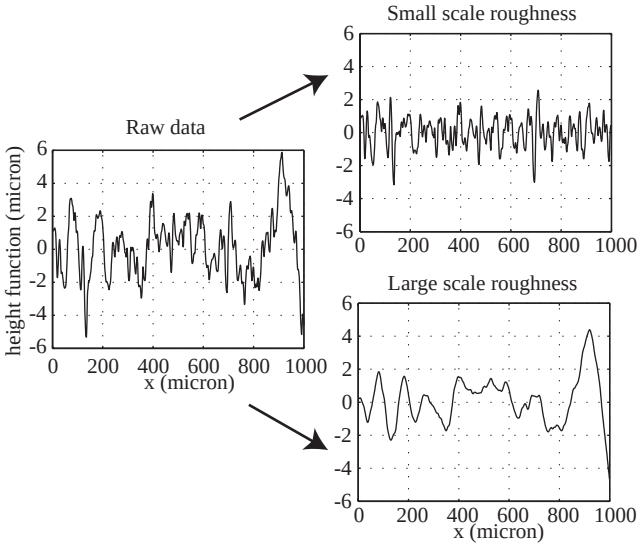

Figure 1 Separation of a mechanically-measured surface-roughness height scan into high-frequency (small-scale) and low-frequency (large-scale) components for the aluminized ground glass surface GGAL120

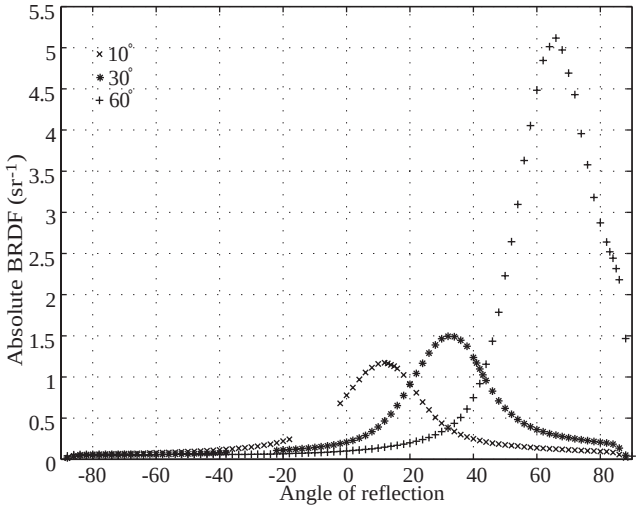

Figure 2 Measured incidence-plane BRDFs for aluminized bead-blasted steel surface BBQAL2 (the smoothest steel surface) for several incidence angles θ_i; λ=550nm

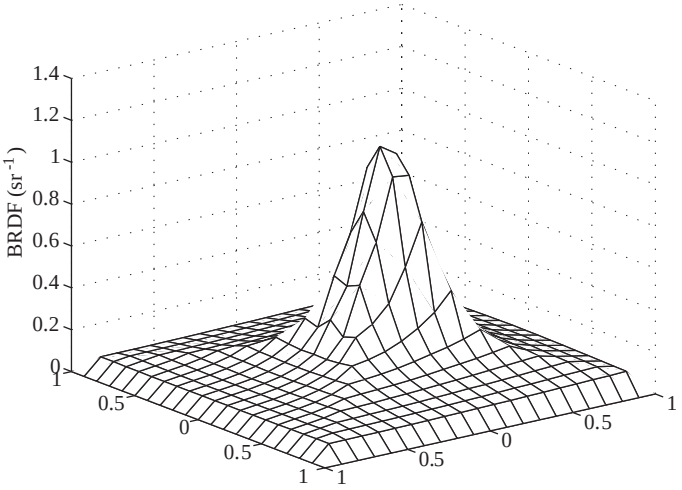

Figure 3 Measured BRDF over the mapped reflection hemisphere for aluminized bead-blasted steel surface BBQAL2 (the smoothest steel surface, slope σ/τ=0.084) for θ_i=10° and λ=550nm

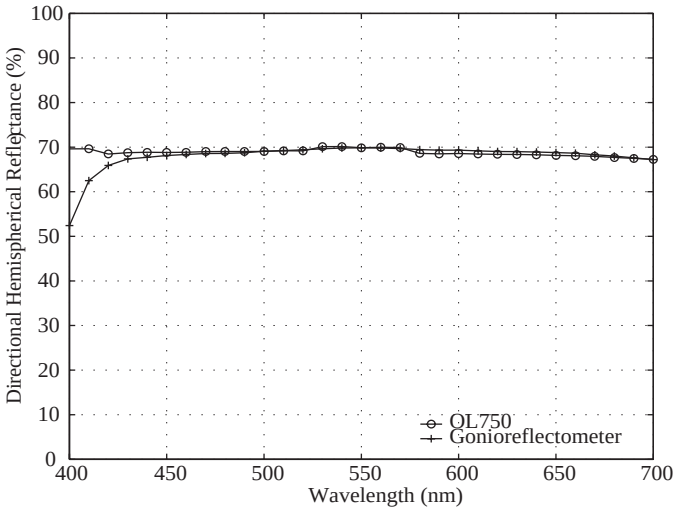

Figure 4 Comparison of directly-measured (OL750) and BRDF-integrated (gonioreflectometer) directional-hemispherical reflectances for aluminized bead-blasted steel surface BBQAL2 (smoothest steel, slope σ/λ=0.084), θ_i =10°

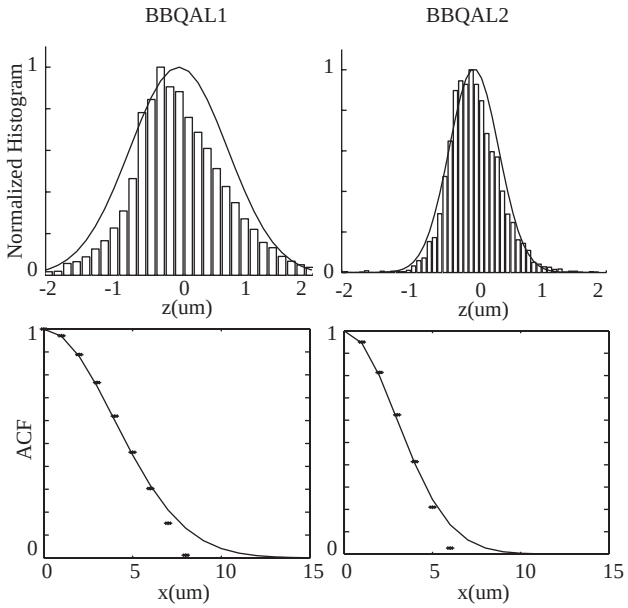

Figure 5 Normalized histogram and autocorrelation function of the small-scale roughness component for aluminized bead-blasted steel surfaces BBQAL1 (roughest, slope σ/τ=0.129) and BBQAL2 (smoothest, slope σ/τ=0.084). The curves are Gaussian distributions.

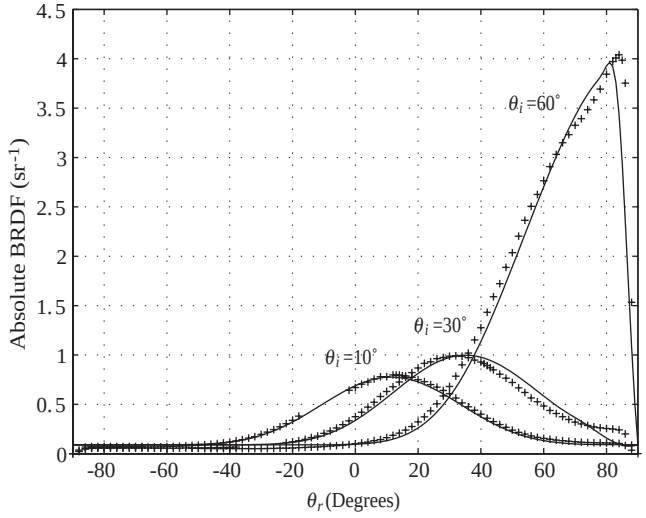

Figure 6 Comparison of measured BRDFs (symbols) and data fitting results (curves) for aluminized bead-blasted steel surface BBQAL1 (roughest, slope σ/τ=0.129), in the plane of incidence, for several incidence angles θ_i; λ=550nm

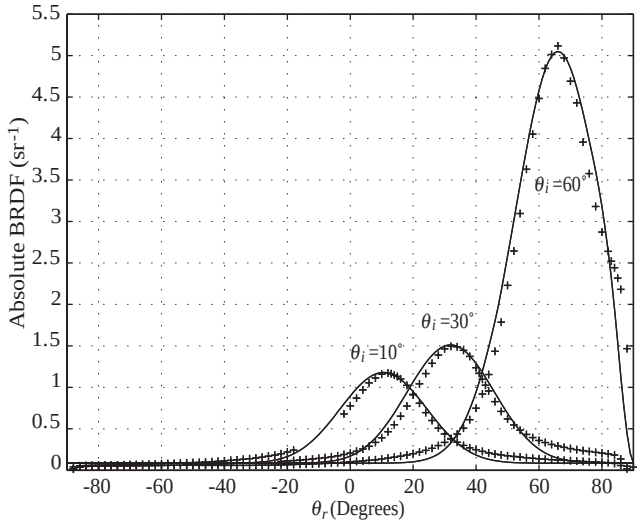

Figure 7 Comparison of measured BRDFs (symbols) and data fitting results (curves) for aluminized bead-blasted steel surface BBQAL2 (smoothest, slope σ/τ=0.084), in the plane of incidence, for several incidence angles θ_i; λ=550nm

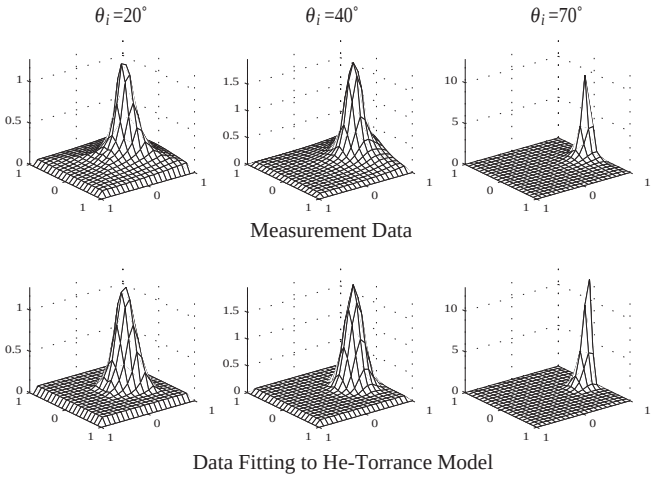

Figure 8 Comparison of measured BRDFs (upper row) and data fitting results (lower row) for aluminized bead-blasted steel surface BBQAL2 (smoothest, slope σ/τ=0.084), over the entire reflection hemisphere, for several incidence angles θ_i; λ=550nm

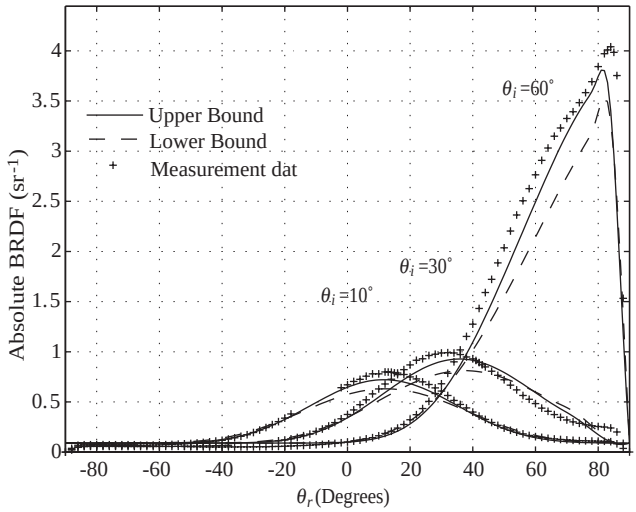

Figure 9 Comparison of measured and predicted BRDFs for aluminized bead-blasted steel surface BBQAL1 (roughest, slope σ/τ=0.129), in the plane of incidence, for several incidence angles θ_i; λ=550nm. Mechanically-measured small-scale roughness values were used for the predictions; upper/lower bounds correspond to the observed roughness variation over the surface.

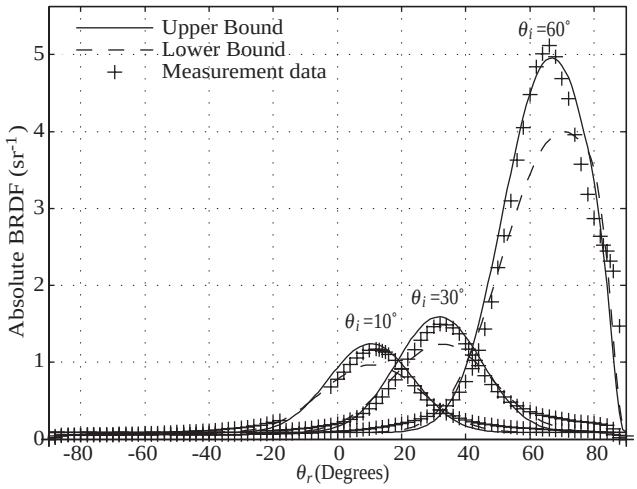

Figure 10 Comparison of measured and predicted BRDFs for aluminized bead-blasted steel surface BBQAL2 (smoothest, slope σ/τ=0.084), in the plane of incidence, for several incidence angles θ_i; λ=550nm. Mechanically-measured small-scale roughness values were used for the predictions; upper/lower bounds correspond to the observed roughness variation over the surface.

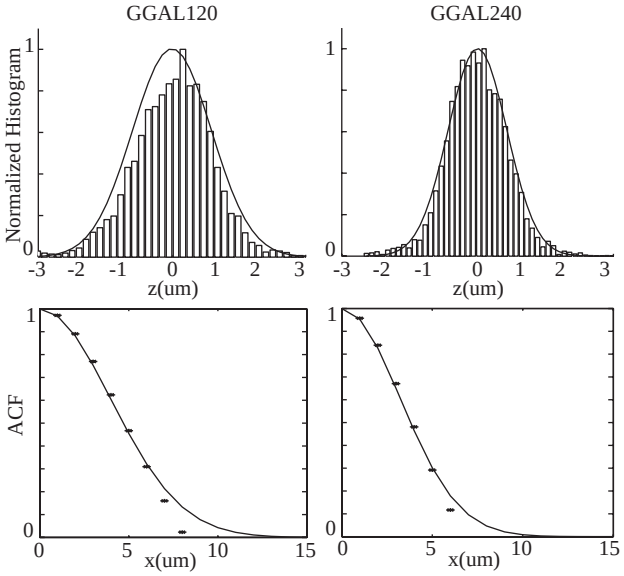

Figure 11 Normalized histogram and autocorrelation function of the small-scale roughness component for aluminized ground glass surfaces GGAL120 (roughest, slope σ/τ=0.154) and GGAL240 (smoothest, slope σ/τ=0.13) The curves are Gaussian distributions.

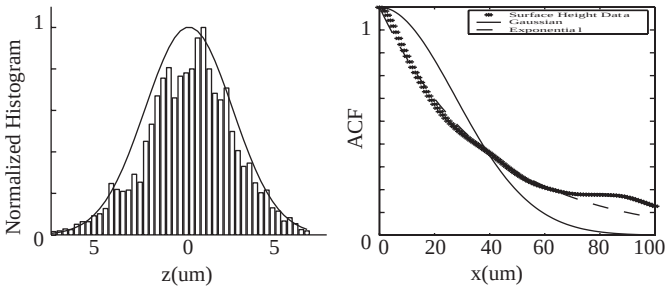

Figure 12 Normalized histogram and autocorrelation function of raw, mechanically-measured, height data for aluminized ground glass GGAL120 (roughest, slope σ/τ=0.154). The raw data was later separated into small-scale (Figure 11) and large-scale components. The solid lines are Gaussian distributions; the dashed line is an exponential distribution.

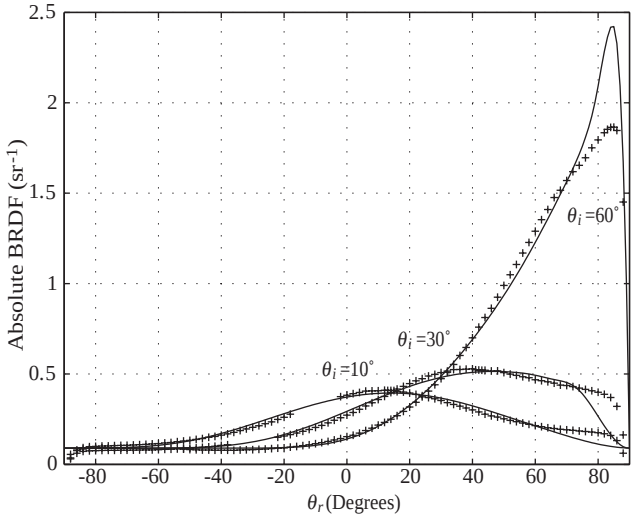

Figure 13 Comparison of measured BRDFs (symbols) and data fitting results (curves) for aluminized ground glass GGAL120 (roughest, slope σ/τ=0.154), in the plane of incidence, for several incidence angles θ_i; λ=550nm

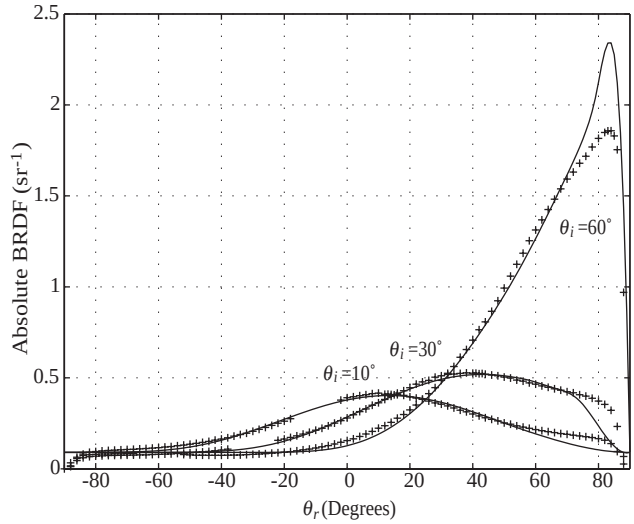

Figure 14 Comparison of measured BRDFs (symbols) and data fitting results (curves) for aluminized ground glass GGAL240 (smoothest, slope σ/τ=0.130), in the plane of incidence, for several incidence angles θ_i; λ=550nm

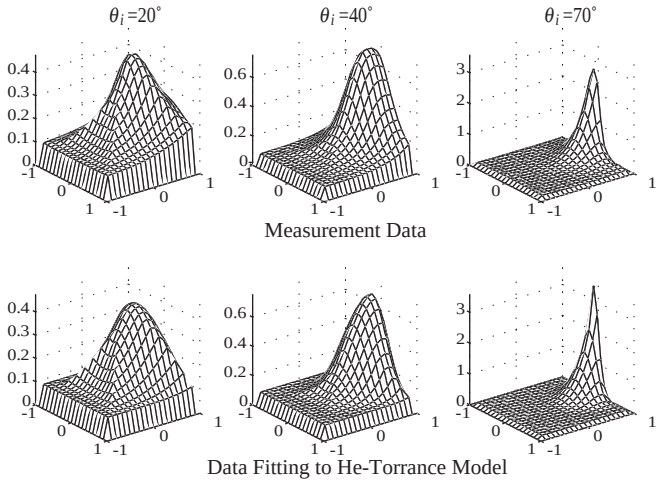

Figure 15 Comparison of measured BRDFs (upper row) and data fitting results (lower row) for aluminized ground glass GGAL120 (roughest, slope σ/τ=0.154), over the entire reflection hemisphere, for several incidence angles θ_i; λ=550nm

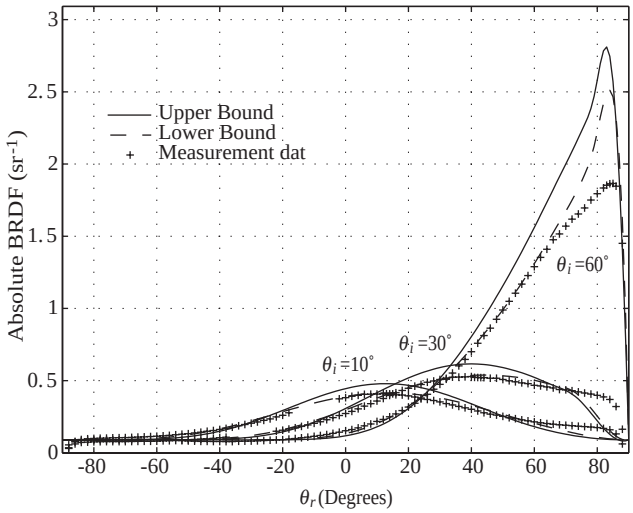

Figure 16 Comparison of measured and predicted BRDFs for aluminized ground glass GGAL120 (roughest, slope σ/τ=0.154) in the plane of incidence, for several incidence angles θ_i; λ=550nm. Mechanically-measured small-scale roughness values were used for the predictions; upper/lower bounds correspond to the observed roughness variation over the surface.

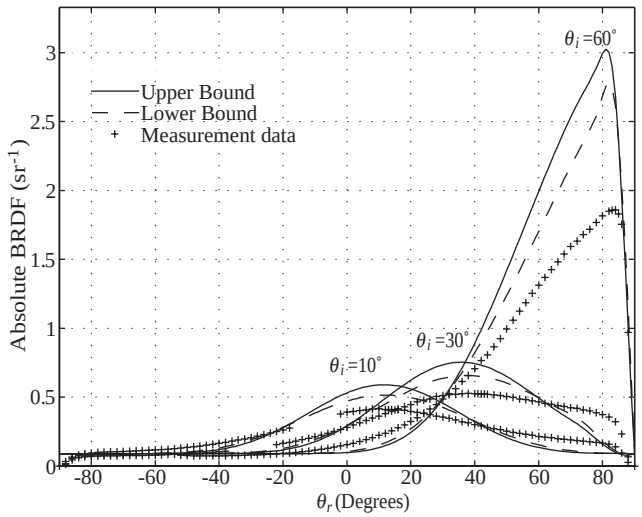

Figure 17 Comparison of measured and predicted BRDFs for aluminized ground glass GGAL240 (smoothest, slope σ/τ=0.130) in the plane of incidence, for several incidence angles θ_i; λ=550nm. Mechanically-measured small-scale roughness values were used for the predictions; upper/lower bounds correspond to the observed roughness variation over the surface.

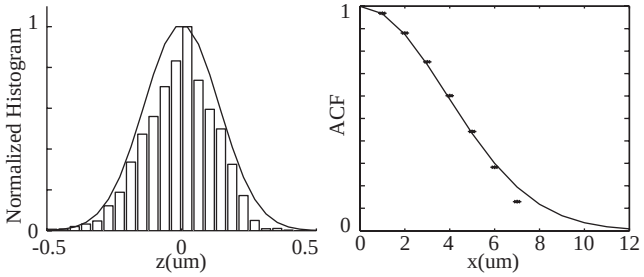

Figure 18 normalized histogram and autocorrelation function of the small-scale roughness component for aluminized acid-etched glass NGGAL (slope σ/τ=0.024). The curves are Gaussian distributions.

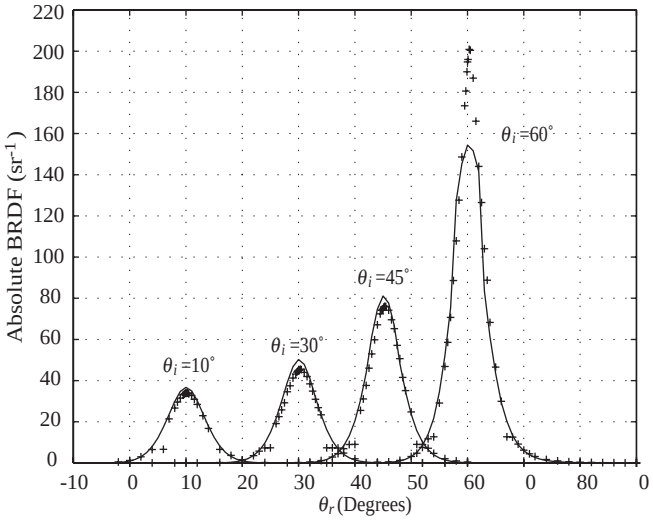

Figure 19 Comparison of measured BRDFs (symbols) and data fitting results (curves) for aluminized acid-etched glass NGGAL (slope σ/τ=0.024), in the plane of incidence, for several incidence angles θ_i; λ=550nm

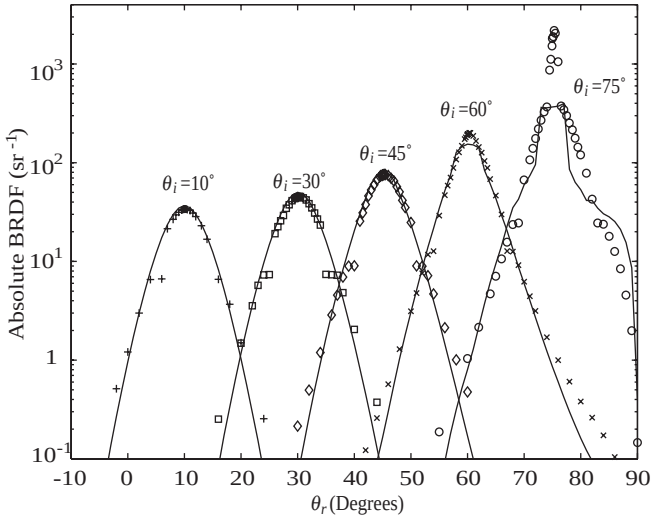

Figure 20 Results from Figure 19 replotted with a logarithmic ordinate: comparison of measured BRDFs (symbols) and data fitting results (curves) for aluminized acid-etched glass NGGAL (slope σ/τ=0.024), in the plane of incidence, for several incidence angles θ_i; λ=550nm.

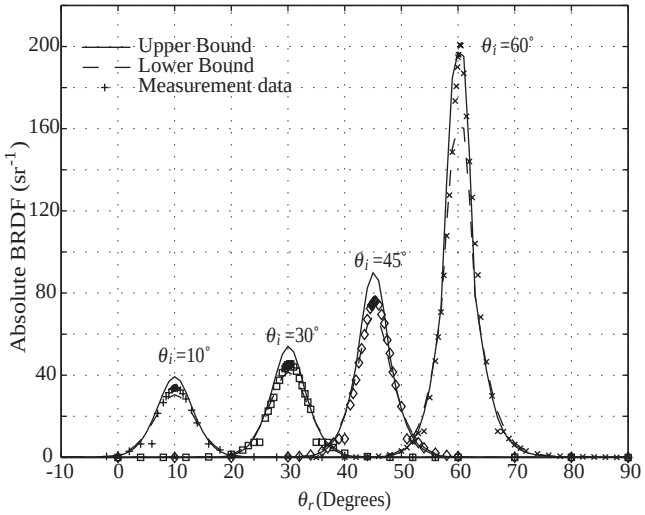

Figure 21 Comparison of measured and predicted BRDFs for aluminized acid-etched glass NGGAL (slope σ/τ=0.024), in the plane of incidence, for several incidence angles θ_i; λ=550nm. Mechanically-measured small-scale roughness values were used for the predictions; upper/lower bounds correspond to the observed roughness variation over the surface.